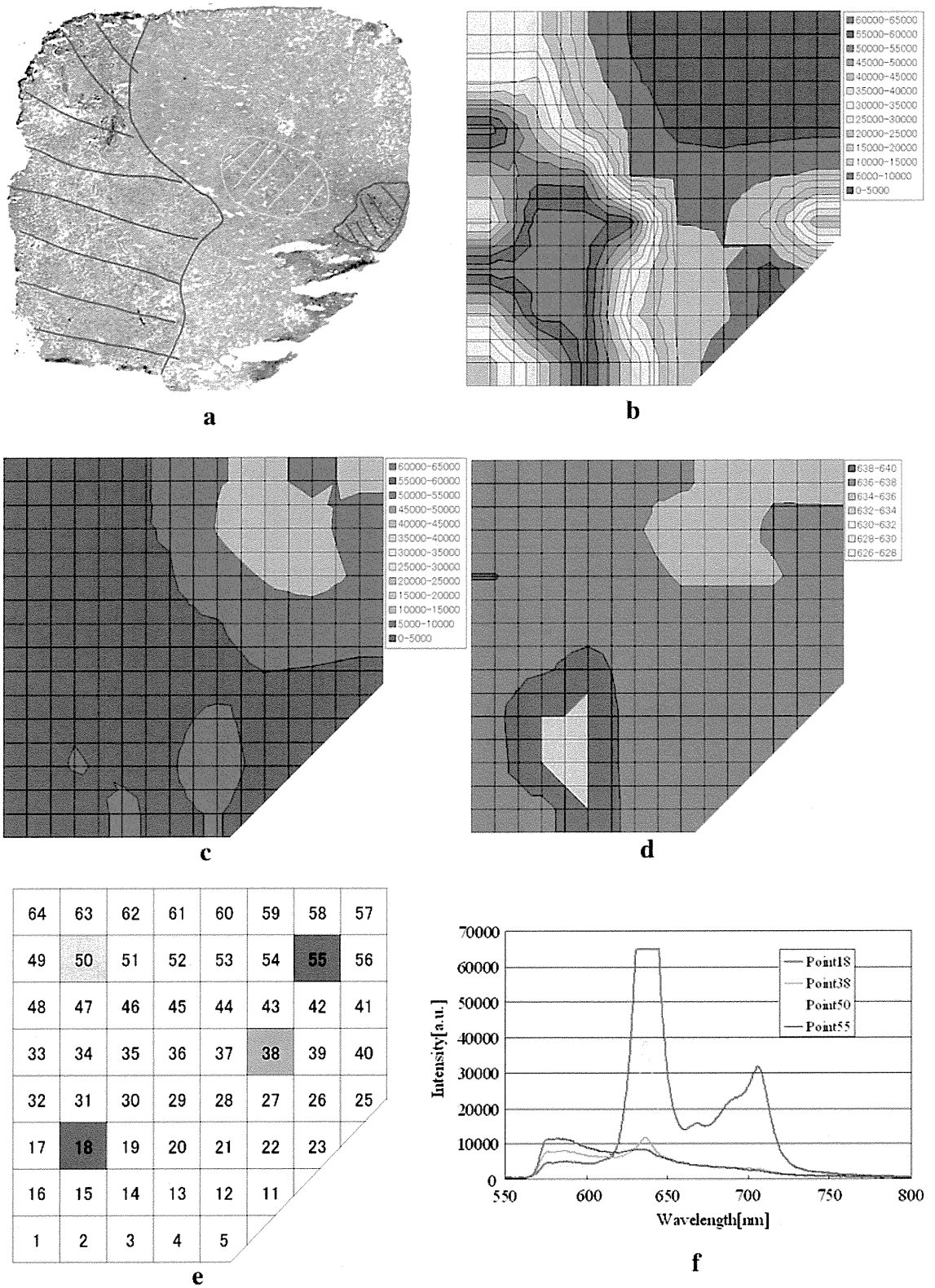

Fig. 5 Results of tissue 5D. **a** Pathological result: this tissue had characteristic tumor distribution (*blue line*) and reactive astrocytes (*yellow line*). **b** Intensity distribution of protoporphyrin IX (PpIX) fluorescence. **c** Intensity distribution at 585 nm. **d** Peak wavelength distribution of PpIX fluorescence. **e** Examples of measured points. **f** Example of measured spectra corresponding to measured points (**e**)

are two possible causes. First, adherent blood on the tissue surface may prevent PpIX fluorescence measurement. Because red blood cells efficiently absorb UV light, which was used as the excitation laser, the light may not reach tissue PpIX [13–15]. In order to avoid damaging cells and changing there characteristics, we did not wash the tissue; however, as much excessive blood as possible had to be removed Second, not enough PpIX accumulated to emit fluorescence. The intake of 5-ALA may depend on the state of the BBB, and this influences the amount of PpIX. Because the BBB was not damaged severely in the low-grade tumor, PpIX may not emit fluorescence in such patients. Actually, tissue 4 was considered an oligodendroglioma, which is classified as grade II according to the World Health Organization classification [16]. Although we cannot control 5-ALA intake, our method can reveal limitations of 5-ALA-induced PpIX fluorescence.

The third group encompassed the false positive case of tissue 5A, which included reactive astrocytes that appear when brain tissue is injured. This false negative finding was also reported by Utsuki et al. [17]. The original astrocyte (not reactive), which is one of the glia cells, has many functions in the brain, such as maintaining brain structure, regulating ion concentration in the extracellular space, and supporting metabolic activity. The most important function of the astrocyte is that it controls the BBB [18, 19]. We hypothesized that the astrocytes changed their characteristics when they became reactive; subsequently, the BBB did not function efficiently, resulting in a higher 5-ALA intake. However, although PpIX fluorescence was detected as false positive, our measurement showed that the spectra of the tissue, including reactive astrocytes, were different from those of the tumor (short-wavelength intensity was high), which may reduce false positive error.

There are certain limitations to our technique. We deliberately changed the exposure time of the spectrometer because fluorescence intensity varied greatly with tissues and exceeded the dynamic range of the spectrometer. This problem prevents comparison among patients and results in an undesirable variety of data. However, the issue can be solved using exchangeable neutral-density filters and some estimation calculations. We developed a modified system that enables maintenance of the same measurement conditions for all patients, and now we measure tissues from various types of glioma using the modified system. Those data will show accurate tumor discrimination and the limitation of 5-ALA-induced PpIX fluorescence. Furthermore, we are working on a robotic system that uses 5-ALA-induced PpIX fluorescence for diagnosis and a midinfrared laser for tumor ablation [20]. The system allows intraoperative tumor identification and ultraprecise ablation. We expect that the method presented in this paper will provide a more accurate intraoperative diagnosis.

Conclusion

We developed a spectrum scanning system that enabled precise comparison of tissue fluorescence spectra with pathological examination. Using the system, we measured 13 brain tissues from five patients and compared fluorescence spectra with pathology. Results showed that there was good correlation between fluorescence distribution and pathological results in high-grade tumor, and there were also false negative and false positive cases. We found that the spectrum of the false positive case, which had reactive astrocytes, was different from tumor spectrum. The results may reduce false positive error and lead to more accurate tumor discrimination PpIX fluorescence.

Acknowledgment This work was supported in part by grant for Translational Systems Biology and Medicine Initiative (TSBMI) and Grant-in-Aid for JSPS Fellows.

References

1. Stummer W, Stepp H, Moller G et al (1998) Technical principles for protoporphyrin-IX-fluorescence guided microsurgical resection of malignant glioma tissue. Acta Neurochir (Wien) 140(10):995–1000
2. Stummer W, Novotny A, Stepp H et al (2000) Fluorescence-guided resection of glioblastoma multiforme by using 5-aminolevulinic acid-induced porphyrins: a prospective study in 52 consecutive patients. J Neurosurg 93(6):1003–1013
3. Stummer W, Pichlmeier U, Meinel T et al (2006) Fluorescence-guided surgery with 5-aminolevulinic acid for resection of malignant glioma: a randomised controlled multicentre phase III trial. Lancet Oncol 7(5):392–401
4. Chung YG, Schwartz JA, Gardner CM et al (1997) Diagnostic potential of laser-induced autofluorescence emission in brain tissue. J Korean Med Sci 12(2):135–142
5. Dailey HA, Smith A (1984) Differential interaction of porphyrins used in photoradiation therapy with ferrochelatase. Biochem J 223(2):441–445
6. Ishihara R, Katayama Y, Watanabe T et al (2007) Quantitative spectroscopic analysis of 5-aminolevulinic acid-induced protoporphyrin IX fluorescence intensity in diffusely infiltrating astrocytomas. Neurol Med Chir (Tokyo) 47(2):53–57
7. Toms SA, Lin WC, Weil RJ et al (2005) Intraoperative optical spectroscopy identifies infiltrating glioma margins with high sensitivity. Neurosurgery 57(4 Suppl):382–391
8. Lin WC, Toms SA, Johnson M et al (2001) In vivo brain tumor demarcation using optical spectroscopy. Photochem Photobiol 73(4):396–402
9. Savitzky A (1964) Smoothing and differentiation of data by simplified least squares procedures. Anal Chem 36(8):1627–1639
10. Wagnieres G (1998) In vivo fluorescence spectroscopy and imaging for oncological applications. Photochem Photobiol 68:603–632
11. Yin D (1996) Biochemical basis of lipofuscin, ceroid, and age pigment-like fluorophores. Free Radic Biol Med 21(6):871–888
12. Eldred GE, Miller GV, Stark WS et al (1982) Lipofuscin: resolution of discrepant fluorescence data. Science 216(4547):757–759
13. Zijlstra WG, Buursma A, van der Roest WPM (1991) Absorption spectra of human fetal and adult oxyhemoglobin,

de-oxyhemoglobin, carboxyhemoglobin, and methemoglobin. Clin Chem 37(9):1633–1638
14. Faber DJ, Mik EG, Aalders MCG et al (2003) Light absorption of (oxy-)hemoglobin assessed by spectroscopic optical coherence tomography. Opt Lett 28(16):1436–1438
15. Faber DJ, Aalders MCG, Mik EG et al (2004) Oxygen saturation-dependent absorption and scattering of blood. Phys Rev Lett 93(2):028102
16. Louis DN, Ohgaki H, Wiestler OD et al (2007) The 2007 WHO classification of tumours of the central nervous system. Acta Neuropathol 114(2):97–109
17. Utsuki S, Oka H, Sato S et al (2007) Histological examination of false positive tissue resection using 5-aminolevulinic acid-induced fluorescence guidance. Neurol Med Chir (Tokyo) 47(5):210–213
18. Janzer RC, Raff MC (1987) Astrocytes induce bloodbrain barrier properties in endothelial cells. Nature 325(6101):253–257
19. Janzer RC (1993) The blood-brain barrier: cellular basis. J Inherit Metab Dis 16(4):639–647
20. Noguchi M, Aoki E, Yoshida D, Kobayashi E, Omori S, Muragaki Y, Iseki H, Nakamura K, Sakuma I (2006) A novel robotic laser ablation system for precision neurosurgery with intraoperative 5-ALA-induced PpIX fluorescence detection. MICCAI 4190:543–550

THE INTERNATIONAL JOURNAL OF MEDICAL ROBOTICS AND COMPUTER ASSISTED SURGERY
Int J Med Robotics Comput Assist Surg 2011; **7**: 214–224.
Published online 28 April 2011 in Wiley Online Library (wileyonlinelibrary.com) **DOI:** 10.1002/rcs.392

ORIGINAL ARTICLE

Intravascular catheter navigation using path planning and virtual visual feedback for oral cancer treatment

Junchen Wang[1,2]*
Takashi Ohya[3,2]
Hongen Liao[2]
Ichiro Sakuma[2]
Tianmiao Wang[1]
Iwai Tohnai[3]
Toshinori Iwai[3]

[1]*School of Mechanical Engineering and Automation, Beihang University, Beijing, China*

[2]*Department of Precision Engineering, School of Engineering, the University of Tokyo, Tokyo, Japan*

[3]*Department of Oral and Maxillofacial Surgery, Graduate School of Medicine Yokohama City University, Yokohama, Japan*

*Correspondence to: Junchen Wang, School of Mechanical Engineering and Automation, Beihang University, Xueyuan Road 37, 100191, Beijing, China.
E-mail: wangjunchen@gmail.com

Accepted: 21 March 2011

Abstract

Background It is tedious and difficult to position a flexible catheter in a target vessel branch within complicated-shaped vessels owing to the lack of real-time visual feedback. Digital subtraction angiography and fluoroscopic guidance are currently used for catheter placement.

Methods The proposed method employs an electromagnetic (EM) tracking system to track a sensor-attached catheter. Vessel centerlines are extracted from the CT angiography image, based on which a navigational information tree is built to facilitate catheter manipulation. A virtual endoscopy technique is adopted to generate virtual intravascular video as visual feedback. Unscented Kalman filtering based image registration is performed to align the EM tracker frame with the anatomical atlas and to envision the target registration error.

Results Preliminary experimental results showed the feasibility and effectiveness of the new method, with navigation accuracy of 1.80 ± 0.85 mm.

Conclusions The proposed method can provide continuous virtual visual feedback to facilitate catheter placement and has the potential for clinical use, with significant reduction in X-ray radiation exposure and doses of contrast agents.

Keywords catheter navigation; virtual intravascular imaging; oral cancer; target registration error

Introduction

The 'retrograde superselective intra-arterial infusion' method is a novel method that has been documented to provide high dose chemotherapeutics for treatment of head and neck cancer (1–6). In this method, a flexible catheter having a pre-bent shape with natural curvature at the tip is inserted into the superficial temporal artery via a small incision on the patient's face. The tip of the catheter needs to be located into the entry of a vessel branch, which may be one of the maxillary artery, the facial artery and the lingual artery, depending on the location of the tumor. When the catheter is well positioned, anti-cancer drugs are injected via the catheter into the target vessel branch for therapy. Because it is relatively easier to pull the catheter out along the superficial temporal artery than to push it in, in real medical intervention a guide wire is used to lead the catheter into

the external carotid artery first, then the guide wire is removed and the catheter is pulled out slowly along the superficial temporal artery until its bent tip enters into the target vessel branch. However, it is a tedious and difficult task to position the catheter. Once the catheter is inserted into the superficial temporal artery, the tip of the catheter cannot be seen directly. Moreover, complicated vessel shapes and friction between the vessel wall and the catheter make it difficult to manipulate the catheter accurately and smoothly. With the current clinical approach, digital subtraction angiography (DSA) is employed to image vessels and the catheter. Contrast agents are injected via the catheter into the blood vessel and DSA images (X-ray imaging) are taken when needed to verify the current position of the catheter. However, DSA images are static 2D images that cannot present surgeons with intuitive and continuous visual feedback. The lack of 3D information in DSA images burdens the surgeon, because he/she has to imagine the spatial relationship between the catheter and surrounding vessels. Based on feelings of hands and experience, the surgeon manipulates the catheter in a near-blind way. These challenges make the placement procedure time-consuming, and excessive X-ray exposure brings health risks to both surgeons and patients. In addition, the dose of contrast agents should be reduced as much as possible.

Vascular imaging and intravascular catheter navigation apply here to facilitate catheter placement. Vascular imaging techniques can be divided into three categories according to their imaging mechanisms, which are optical-based, acoustic-based and X-ray-based vascular imaging. The first category, optical-based vascular imaging (7) visualizes vasculature *in vivo* by detecting the fluorescent signals induced by vascular contrast agents injected into the vessels of interest. However, the visualization procedure is time-consuming and can only be done offline, which is not appropriate for intraoperative use. The second category, acoustic-based vascular imaging includes vascular ultrasound and optoacoustic imaging (8). Medical ultrasound imaging systems provide real-time ultrasound images (2D or 3D) of living tissue by emitting echoes and detecting the reflected signals. Different tissue types thus can be differentiated in the ultrasound image according to their different sound impedance characteristics. Furthermore, Doppler ultrasound (9) allows the evaluation of vascular flow and can be used in the diagnosis of peripheral vascular disease. However, the low quality and resolution of ultrasound images bring difficulties in image understanding and locating surgical instruments. Moreover, ultrasound is useless if the vessel to be visualized is deep below the skin or is obstructed by bones (in our case). Another vascular ultrasound imaging technique is intravascular ultrasound (IVUS) (10). In IVUS a specially designed catheter with a miniaturized ultrasound probe attached to the distal end of the catheter is inserted into a blood vessel, which allows observation from inside vessels. Unfortunately it cannot help in our case. In optoacoustic imaging, short laser pulses are directed to human tissue of interest to generate ultrasound transients by means of the thermoelastic effect. These ultrasound transients can be detected by an ultrasound transducer and synthesized to an image. Because it is possible to irradiate only the tissue of interest by choosing the wavelength of the laser pulses, the resulting image has high contrast compared with the conventional ultrasound image. However, limited by the propagation distance of the laser in tissue, the visualization depth is only a few centimeters. The last category, X-ray-based vascular imaging, includes DSA (11) and CT angiography (12). DSA is a type of fluoroscopy technique used in endovascular interventions to visualize blood vessels and locate the catheter. By injecting contrast agents, clear DSA images containing vessels are produced by subtracting 'pre-contrast' images from 'post-contrast' images. The demerits of DSA include the administration of contrast agents, the lack of 3D information, and the radiation exposure. CT angiography can produce high-quality 3D CT images with blood vessels clearly presented. Vessel models can be further created from 3D CT angiography images which will serve as an anatomical atlas during surgical navigation. Nevertheless, CT angiography images are preoperative images which may suffer from inconsistencies with intraoperative tissue.

Regarding intravascular catheter navigation, electromagnetic (EM) tracking based catheter navigation has been reported many times by both clinicians and technicians. Hautmann *et al.* reported a study to assess the usability, accuracy, and safety of electromagnetic navigation for flexible bronchoscopy in a clinical setting (13). Tanase *et al.* presented an electromagnetic navigation system for locating a guide wire in intravascular interventions by overlaying a virtual indicator of the guide wire motion on a pre-taken X-ray image (14). Solomon *et al.* superimposed a tracked 6 French catheter on the CT image of the chest to navigate the catheter within the heart and the great vessels (15). Schneider *et al.* compared clinically a nonfluoroscopic catheter navigation system (LocaLisa, Medtronic EP Systems, Minneapolis, MN, USA) with the conventional approach for ablation of atrial flutter and reported that the LocaLisa system significantly reduced fluoroscopy time (16). Ramcharitar *et al.* integrated multislice computed tomography with magnetic navigation to facilitate percutaneous coronary interventions without contrast agents (17). However, in these previous studies, no more information was provided other than the overlay of the catheter tip on a 2D/3D image. In this present study, by combining EM tracking with virtual intravascular imaging and path planning, we aim to navigate the flexible catheter by providing intuitive visual feedback and accurate navigational data, and hence facilitate catheter placement with significant reduction in X-ray radiation exposure and contrast agents dosing.

Materials and Methods

Real medical intervention can be divided into two steps, here named SP1 and SP2. In SP1, the catheter

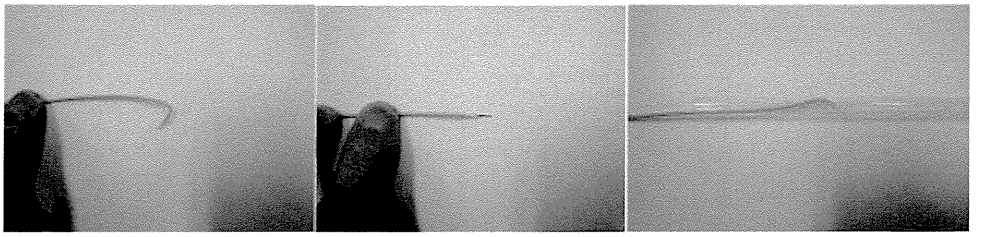

Figure 1. (a) Natural shape of the catheter. (b) Catheter with guide wire in the lumen (in SP1). (c) Half-restored bent tip (in SP2). For demonstration, a drinking straw is used to emulate a blood vessel

(Figure 1(a)) is guided by a guide wire from the incision entry on the patient's face to the external carotid artery. Because the guide wire is inserted into the lumen of the catheter, the catheter is straightened and looks like a tiny flexible endoscope (Figure 1(b)). In SP2, the guide wire has been removed and the catheter is restored to its natural shape. Owing to the constraint of the vessel wall, the bent tip is only half-restored (Figure 1(c)). The surgeon pulls the catheter out along the external carotid artery and tries to position it into the target vessel branch. The catheter shape at the different steps is illustrated in Figure 1. Catheter placement in SP2 is more difficult than in SP1 and most of the X-ray exposure occurs in SP2, thus we follow different navigation strategies in SP1 and SP2.

Catheter modeling

To visualize the catheter, we first give its mathematical model and then generate its surface rendering model which can bend as the true one. The pose of the bent tip is very important for placement, so there is no need to model the whole catheter body, only the bent tip. The catheter is a bendable tube (Φ 1.33 mm). If we can determine the centerline of this tube, the shape can be recovered from it. So the key point is to determine the pose and shape of the catheter centerline. For this purpose, we attach two 5DOF (degree of freedom) electromagnetic sensor coils (Φ 0.55 mm $\times$ 8 mm, referred to as sensor A and B) to the catheter, with the configuration shown in Figure 2(a). Although the sensors are attached outside the lumen for easy reuse, the total size of the sensor-attached catheter is only 1.88 mm in diameter, which is smaller than that of the target vessel. The pose of a 5DOF sensor (center and axial orientation) with respect to a reference frame can be acquired by an EM tracking system in real time. Owing to the lack of one DOF, rotation around the axial direction of the sensor cannot be detected. That is why we need two noncollinear sensors to locate the bent tip of the catheter unambiguously. As shown in Figure 2(b), we use a 6×1 vector $\boldsymbol{f} = (\boldsymbol{o}^{\mathrm{T}}, \boldsymbol{p}^{\mathrm{T}})^{\mathrm{T}}$ to represent a 5DOF sensor frame (sensor reading) where $\boldsymbol{o}$ and $\boldsymbol{p}$ are 3×1 vectors representing the center and the axial direction of the sensor, respectively. Thus we have the two sensor readings $\boldsymbol{f}_A = (\boldsymbol{o}_A^{\mathrm{T}}, \boldsymbol{p}_A^{\mathrm{T}})^{\mathrm{T}}$ and $\boldsymbol{f}_B = (\boldsymbol{o}_B^{\mathrm{T}}, \boldsymbol{p}_B^{\mathrm{T}})^{\mathrm{T}}$, which are directly determined by an EM tracking system. The shape between A and B can be predicted using spline interpolation (18) according to $\boldsymbol{f}_A$ and $\boldsymbol{f}_B$. When sensor readings of the two sensors are updated, the shape of the catheter model will also be changed to reflect the truth. However, the centers of the sensors $\boldsymbol{o}_A$ and $\boldsymbol{o}_B$ are not on the centerline of the real catheter (take radii of both the catheter and the sensors into account) which will result in inaccurate catheter tracking. To overcome this problem, catheter–sensor calibration should be performed. By calculating the following cross-products:

$$\boldsymbol{n}_{AB} = \boldsymbol{p}_A \times \boldsymbol{p}_B \tag{1}$$

$$\boldsymbol{t}_A = \boldsymbol{p}_A \times \boldsymbol{n}_{AB} \tag{2}$$

$$\boldsymbol{t}_B = \boldsymbol{p}_B \times \boldsymbol{n}_{AB} \tag{3}$$

we get $\boldsymbol{t}_A$ and $\boldsymbol{t}_B$ pointing towards the centerline from $\boldsymbol{o}_A$ and $\boldsymbol{o}_B$, respectively (Figure 2(b)). Moving $\boldsymbol{o}_A$ and $\boldsymbol{o}_B$ along $\boldsymbol{t}_A$ and $\boldsymbol{t}_B$ by the sum of r_s and r_c aligns $\boldsymbol{o}_A$ and $\boldsymbol{o}_B$ with the catheter centerline, where r_s and r_c are the radii of the sensor and the catheter, respectively. By means of the catheter–sensor calibration, spatial information including the poses of the catheter tip and the catheter body is available during navigation. This information is used to generate the flexible surface rendering model of the catheter (Figure 2(c)) which is overlaid on the anatomical atlas for image guidance.

Path planning and navigational information tree

As with other image-guided interventions, an anatomical atlas is necessary for navigation. The blood vessels of interest are segmented from the patient's CT angiography image and the surface rendering model of the vessels, which serves as the anatomical atlas during navigation, is constructed from the segmented vessel image. To achieve effective navigation, it is assumed to have some predefined paths that can store local navigational data to guide catheter placement. The centerline of the vessel is a good choice as a guidance path.

The segmented vessel image is a binary image of 1s and 0s which represent the interior and the exterior of the vessels, respectively. To extract vessel centerlines, the Euclidean distance transformation of the binary image is firstly created (19). As a result, a distance mapping volume dataset is available. Then the vessel centerlines of interest

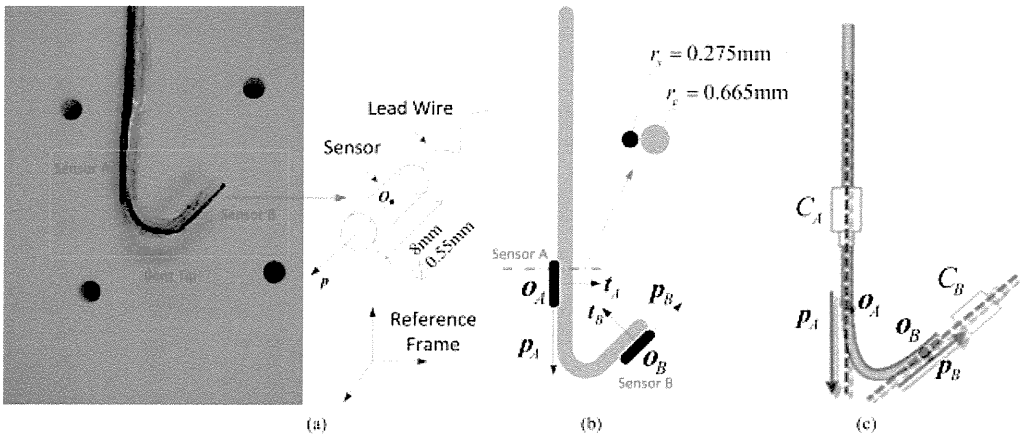

Figure 2. (a) Sensor-attached catheter. (b) Mathematical model of the catheter. (c) Surface rendering model of the catheter with two virtual cameras C_A and C_B

are extracted based on the distance mapping volume using the method proposed by Wan *et al.* (20). The resulting centerline is a collection of discrete voxels. Lastly, the discrete centerline is smoothed using the cubic-spline fitting algorithm (21). Let $\boldsymbol{v}_i = (x_i, y_i, z_i)^{\mathrm{T}}$, $i = 1, 2, \cdots, N$ represent the coordinates of the successive voxel which is on the discrete centerline, the smoothed centerline $\boldsymbol{v}(t) = (f_x(t), f_y(t), f_z(t))^{\mathrm{T}}$ can be obtained by solving the following optimization problem:

$$\begin{pmatrix} f_x(t) \\ f_y(t) \\ f_z(t) \end{pmatrix} = \begin{pmatrix} \arg\min_{f_x} p\sum_{i=1}^{N} w_i(x_i - f_x(t_i))^2 \\ \quad +(1-p)\int_{t_1}^{t_N}[f_x''(t)]^2\mathrm{d}t \\ \arg\min_{f_y} p\sum_{i=1}^{N} w_i(x_i - f_y(t_i))^2 \\ \quad +(1-p)\int_{t_1}^{t_N}[f_y''(t)]^2\mathrm{d}t \\ \arg\min_{f_z} p\sum_{i=1}^{N} w_i(x_i - f_z(t_i))^2 \\ \quad +(1-p)\int_{t_1}^{t_N}[f_z''(t)]^2\mathrm{d}t \end{pmatrix}, t_i = i \quad (4)$$

where $f(t)$ is a spline function, w_i is the error weight of the i^{th} voxel on the discrete centerline, p is the smoothness coefficient which balances the tradeoff between 'fitting' and 'interpolation'. The i^{th} voxel of the discrete centerline is assigned with the reciprocal of its corresponding distance transform value as w_i. This ensures that in the narrow part of the vessel, the error tolerance becomes small and in the thick part, a larger error is permitted. The smoothed centerline is a good tradeoff between smoothness and fidelity (Figure 3(a)). Based on the smoothed centerlines, a data structure called the navigational information tree (NIT) is built to store local navigational data used for catheter guidance as shown in Figure 3(b). Each point on the centerline corresponds with a node in the NIT. The node of the NIT accommodates the local information including the coordinates of the current node, the name of the vessel and the tangent vector of the centerline at the current node. It is easy to incorporate other information into the node if needed. Some operations on the NIT are also defined, such as finding the nearest node given the position of the catheter tip, traversing back and forth between nodes, etc. These operations will be invoked during navigation.

Virtual intravascular imaging

Our method aims at providing surgeons with intuitive information about the catheter placement. It is preferred to obtain an intravascular image when manipulating the catheter but it is impossible to attach a CCD camera on the catheter tip to provide real-time intravascular video during placement. Even if possible, nothing other than blood would be observed. However, we can set up two virtual cameras C_A and C_B on the surface rendering model of the catheter to provide real-time virtual intravascular video during tracking (22). As shown in Figure 2(c), the principal axis of camera C_A points in the same direction as $\boldsymbol{p}_A$ and the center of C_A is constrained to move only along $\boldsymbol{o}_A - \boldsymbol{p}_A$. C_B has a similar setting. Besides the two virtual cameras, a third virtual camera C_V is also set with its motion constrained along the vessel centerline and its principal axis pointing along the tangent vector to the centerline. Given a position and a direction, the virtual endoscopy technique is used to render the virtual image concerning the interior of the vessel and successive virtual images form a virtual intravascular video stream. Functionally speaking, C_A provides the view seen along the catheter body; C_B provides the view seen along the bent tip; the position of C_V is updated according to the tracked catheter so that the surgeon can observe the catheter tip from inside the vessel. In this way surgeons can acquire continuous intuitive visual feedback concerning what they are doing. Figure 4 demonstrates the formation of the virtual intravascular video and some screenshots during navigation.

Image registration and TRE visualization

Image registration should be performed to align the EM tracker frame with the anatomical atlas. The patient

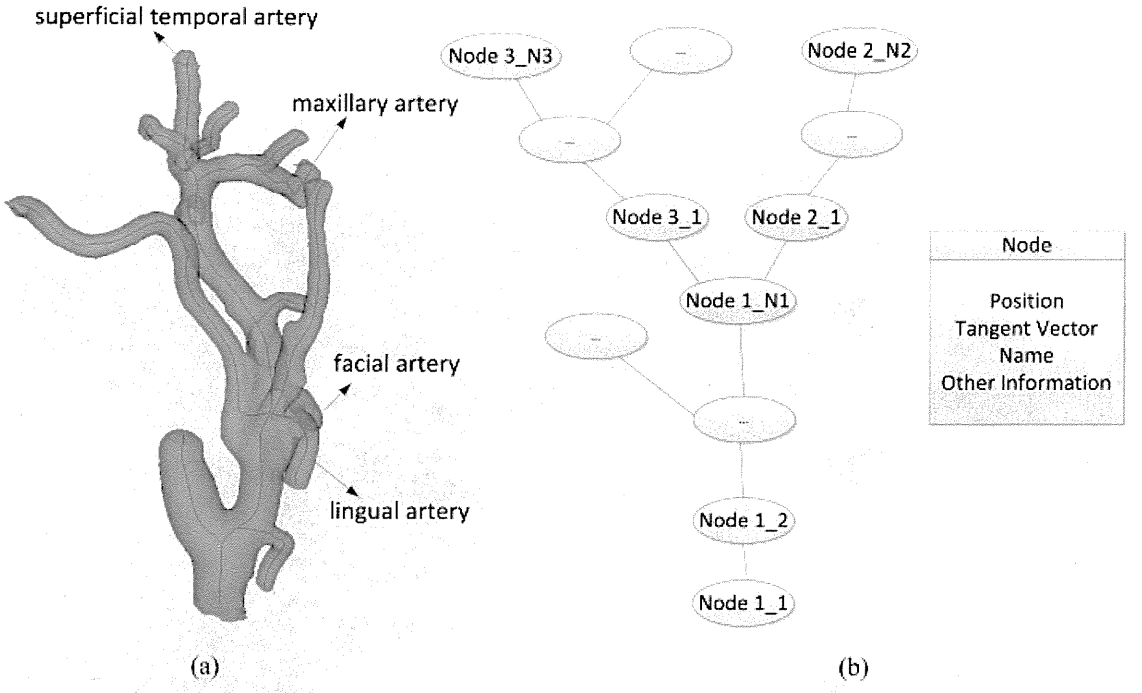

Figure 3. (a) Surface rendering model of vessels with smoothed centerlines. (b) Data structure of the navigational information tree

undergoes CT angiography scan with skin markers configured around the head and neck area. The centers of the skin markers (fiducial points) are identified both in the EM tracker frame by a tracked stylus and in the CT image from which the anatomical atlas is derived. A point-based algorithm is employed to estimate the transformation matrix from the CT image to the EM tracker frame. Also called the absolute orientation problem, there exists a closed-form solution when the datasets are excited by additive isotropic Gaussian noise (23–26). Unfortunately, the anisotropic Gaussian noise characteristic of EM tracking systems has been reported (27) and under this assumption, the closed-form solution for the absolute orientation problem is not optimal. Thus the unscented Kalman filtering (UKF)-based algorithm is employed (28). It has been proved that the UKF-based algorithm outperforms Horn's algorithm (25, 26) in the presence of anisotropic Gaussian noise. Furthermore, the UKF-based registration method can, in addition, estimate the variance of the transformation matrix, which can be used to envision the target registration error (TRE) (29). Before applying UKF to the image registration, the noise characteristics for localizing the fiducials in the two frames (i.e. the EM tracker frame and the CT image) should be investigated.

Fiducial localization error in the EM tracker frame

A calibration device (Figure 5(a)) with $10 \times 11 \times 6$ precisely-located (position error 0.05 mm, guaranteed mechanically) holes which form a canonical frame is registered with the EM tracker frame. The radius of the hole is the same as that of a stylus whose tip can be tracked by the EM tracking system. Some special devices are designed to guarantee consistent orientation of the stylus when inserted into the hole. By inserting the stylus into each one of the 660 holes, the coordinates of the 660 holes in the EM tracker frame are acquired. On the other hand, their canonical coordinates are already known. Then the transformation matrix from the canonical frame to the EM tracker frame is estimated using the 660 fiducial holes. After that, the fiducial registration error (FRE) on each hole is calculated and visualized as shown in Figure 5(b). Although the measurement accuracy of the EM tracking system deteriorates if the sensor coil is far away from the field generator (27), in our case the surgical space is very small and the field generator of the EM tracking system is configured fairly close to the surgical site, therefore we assume that the FRE is white noise and independent of the location in surgical space. Moreover, its three components (errors in x, y, z directions) are also assumed to be independent (i.e. the variance matrix of the FRE is a diagonal matrix). Under these assumptions, the variance of the FRE, referred to as Σ_{EM}, can be estimated from the 660 observations (samples of the FRE). Because the calibration device has high position accuracy and the number of fiducial holes is large, the FRE of the device-tracker registration can be regarded as the fiducial localization error (FLE) of the EM tracking system.

Fiducial localization error in the CT image

To localize fiducials in the CT image, an interactive means is used by choosing centers of the skin makers presented in the CT image. Also, independent white noise is assumed.

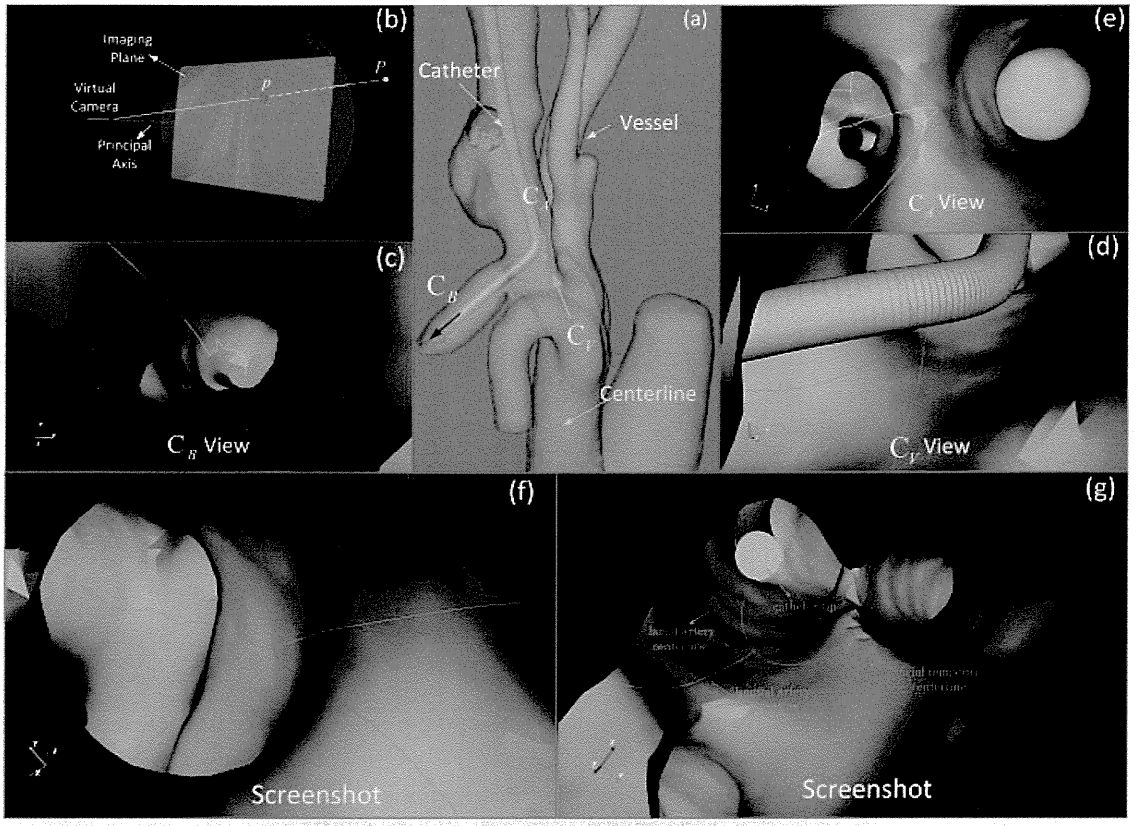

Figure 4. (a) Navigation scene. (b) Imaging process of the virtual camera. (c) Virtual image by C_B. (d) Virtual image by C_V. (e) Virtual image by C_A. (f) and (g) screenshots of the intravascular video

The same skin marker in the CT image is re-localized using our navigation system 1000 times and the variance of the FLE, referred to as Σ_{CT}, is estimated statistically. Then the resulting variance matrix is enlarged 10-fold to compensate the white noise assumption.

TRE visualization

We use a 6×1 vector $f = (r^T, t^T)^T$ to represent a rigid transformation between two rigid frames, where r is a rotation vector and t is a translation vector. Due to the existence of the anisotropic Gaussian FLE in both the EM tracker frame and the CT image, the UKF-based registration algorithm is used to estimate the optimal rigid frame $\hat{f}$ and its variance $\hat{\Sigma}$. Several pairs of matched fiducial points together with Σ_{EM} and Σ_{CT} are input and as the output of the algorithm, we obtain $\hat{f}$ and $\hat{\Sigma}$. $\hat{\Sigma}$ is further used to estimate the distribution of the TRE up to the second-order Taylor expansion in target space (i.e. the CT image) (30, 31). Then the TRE map, which visualizes the distribution of the TRE, is created to depict the RMS (root mean square) error when a point in the EM tracker frame is mapped to the CT image (target space). The TRE map could be overlaid on the anatomical atlas during the navigation to indicate the possible error caused by the image registration. Note should be taken that the TRE distribution also depends on the spatial configuration of the skin markers. Therefore by envisioning the TRE, we know whether the current configuration of the skin markers is degenerating or not.

Navigation workflow

The proposed navigation procedure is divided into two parts: preoperative processing and intra-operative processing.

Preoperative processing

- The preoperative CT angiography image of the patient's head is acquired from which the vessels of interest and the skull are segmented.
- The surface rendering models of the skull and vessels are generated from the segmented images using the marching cube algorithm.
- The segmented vessel image is further processed to create its transform distance volume.
- Based on the transform distance volume, the vessel centerlines of interest are extracted as the guidance paths.
- The centerlines are smoothed and then curvature-adaptive resampling on the smoothed centerlines is performed to generate the NIT nodes, which are further connected to form the NIT according to the vessel shapes.

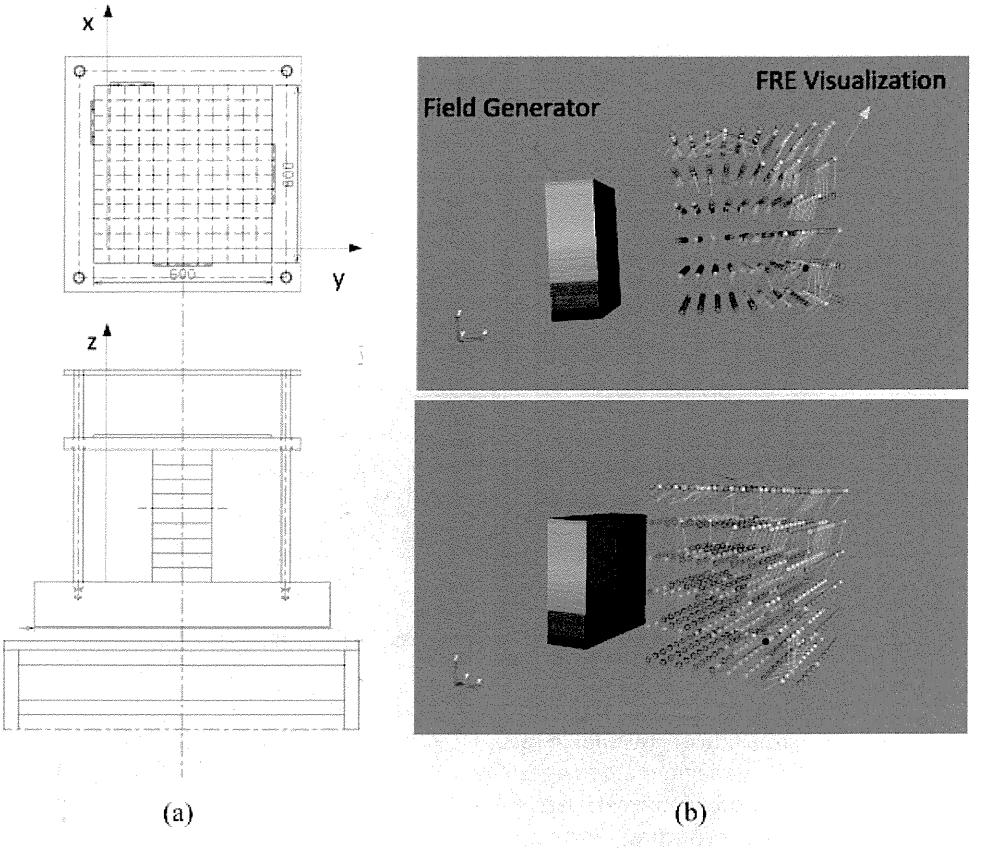

Figure 5. (a) Calibration device. A marble plate with 10 x 11 accurate holes can be fixed at 6 different positions along its z axis with spacing 50 mm. (b) FRE visualization. Colorful balls represent locations of the holes and vectors represent FRE errors at 660 locations. Note that the length of the vector is enlarged 10 times for better visualization

- Relevant operations on the NIT are defined (e.g. finding the nearest NIT node given a position in the CT image).

The segmented skull image is needed, because (1) the skin markers for image registration are attached on the skin which is near to the skull, and (2) it is easy to understand the relative position of the catheter in the presence of the skull.

Intra-operative processing

The intra-operative navigation includes SP1 and SP2 as described previously. First, the anatomical atlas consisting of the skull and the vessels is loaded and displayed on the monitor. Then the patient's head is fixed, avoiding shift during the intervention, and the image registration is performed. After image registration, SP1 is performed. In SP1, we regard the catheter with guide wire as a tiny endoscope whose real-time virtual intravascular video is provided by the virtual camera C_B. For every tracking frame:

- Obtain and save sensor frames f_A and f_B, update the surface rendering model of the catheter.
- Generate the virtual intravascular video of C_B to guide placement.
- Interrogate the NIT to find the nearest NIT node and display the information stored in it.

When SP1 ends, the catheter has entered into the external carotid artery, the guide wire is then removed and SP2 starts:

- For every tracking frame, repeat as in SP1 but instead of C_B, use C_V to observe the bent tip to guide placement.
- When the bent tip is positioned into the target vessel branch, use C_B and C_V to confirm the tip direction.

A final DSA image should be taken for verification because we cannot solely believe any navigation system without real-time imaging modalities.

Results

Experimental setting and procedure

To evaluate the new method, a phantom experiment was designed and performed. The phantoms used in the experiment are a skull phantom and a resin vessel phantom consisting of the superficial temporal artery, the maxillary artery, the facial artery and the lingual artery (Figure 6). The phantoms were created from the CT angiography image of a real patient, using a 3D printer, so they have similar shapes to the real ones. The CT image of the phantoms with skin markers for image registration was acquired at a resolution of 512 × 512 × 258, pixel spacing of 0.43 mm and slice spacing of 0.7 mm.

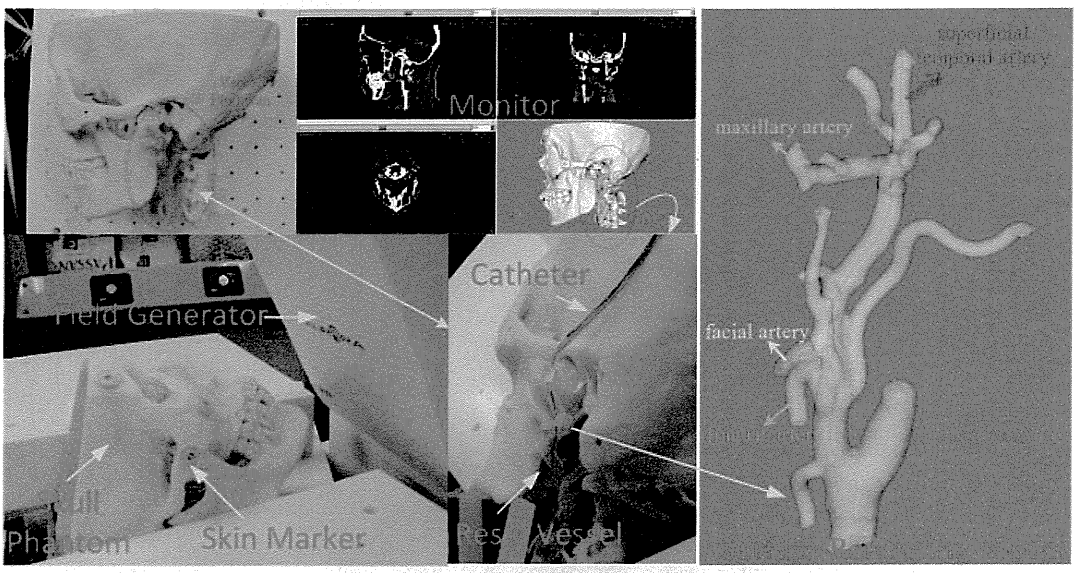

Figure 6. (a) Experiment scene. (b) Objective vessels. In the experiment, the facial artery was chosen as the target branch

Image segmentation was performed to obtain the skull image and vessel image using 3DSlicer (available at http://www.slicer.org/). Based on the segmented images, the anatomical atlas and the navigational information tree were created. An EM tracking system (Aurora; Northern Digital; Waterloo, ON, Canada) was employed to track the sensor-attached catheter. In our case, the surgical site is the head and neck area, so the surgical space was limited to a small space. The field generator of the Aurora system was configured so that the surgical space was within the volume of -100 mm $\leq$ x, y $\leq$ 100 mm, -150 mm $\leq$ z $\leq$ -50 mm in the EM tracker frame. Five pairs of matched fiducial points for image registration were identified in the CT image using the navigation software and in the EM tracker frame using an Aurora 6DOF probe (a stylus). The variance of the estimated transformation matrix was utilized to estimate the target registration error. When the registration procedure was finished, a guide wire was inserted through the catheter and the navigation procedure SP1 was started. When the catheter reached the external carotid artery, the guide wire was removed and SP2 was started.

Image registration result

The variance matrices of the FLE in the EM tracker frame and the CT image were estimated using the proposed methods and the results are shown in (5). Thus we have the RMS of the FLE in the EM tracker frame calculated as RMS $= \sqrt{\text{Trace}(\Sigma_{EM})} = 0.73$ mm, which agrees with the official product specification of the Aurora system. The TRE map covering the whole surgical space was created according to the result of the UKF-based registration as shown in Figure 7. The blue area indicates relatively small RMS errors and the configuration of the skin markers was designed to ensure that the surgical site was located in the blue area.

$$\Sigma_{EM} = \begin{pmatrix} 0.13 & 0 & 0 \\ 0 & 0.10 & 0 \\ 0 & 0 & 0.31 \end{pmatrix},$$

$$\Sigma_{CT} = \begin{pmatrix} 0.24 & 0 & 0 \\ 0 & 0.77 & 0 \\ 0 & 0 & 0.38 \end{pmatrix} \quad (5)$$

Navigation result

Navigation on the phantom was carried out to evaluate the effectiveness and accuracy of the method. Effectiveness means the intervention can be achieved with minimal X-ray exposure and time, which in our opinions relies on intuitive visual feedback and accurate tracking. We asked a professional surgeon to place the catheter with the help of our system and the catheter was smoothly positioned into the right place within 5 minutes (navigation time: SP1+SP2). For conventional intervention without navigation, the time for catheter placement is from 20 minutes to 2 hours depending on the patient and the skills of the surgeon. The navigation procedure is recorded and explained in Figure 8(a).

As a preliminary accuracy assessment, the trace of the catheter tip (Figure 8(b)) and the distance between the catheter tip and the vessel centerline were recorded at the Aurora tracking frequency in SP1. We calculated the mean and standard deviation of the distance, which was 1.80 ± 0.85 mm. This result meets the clinical need according to professional clinicians.

Discussion and Conclusion

We proposed a novel catheter navigation method and implemented a prototype navigation system for oral

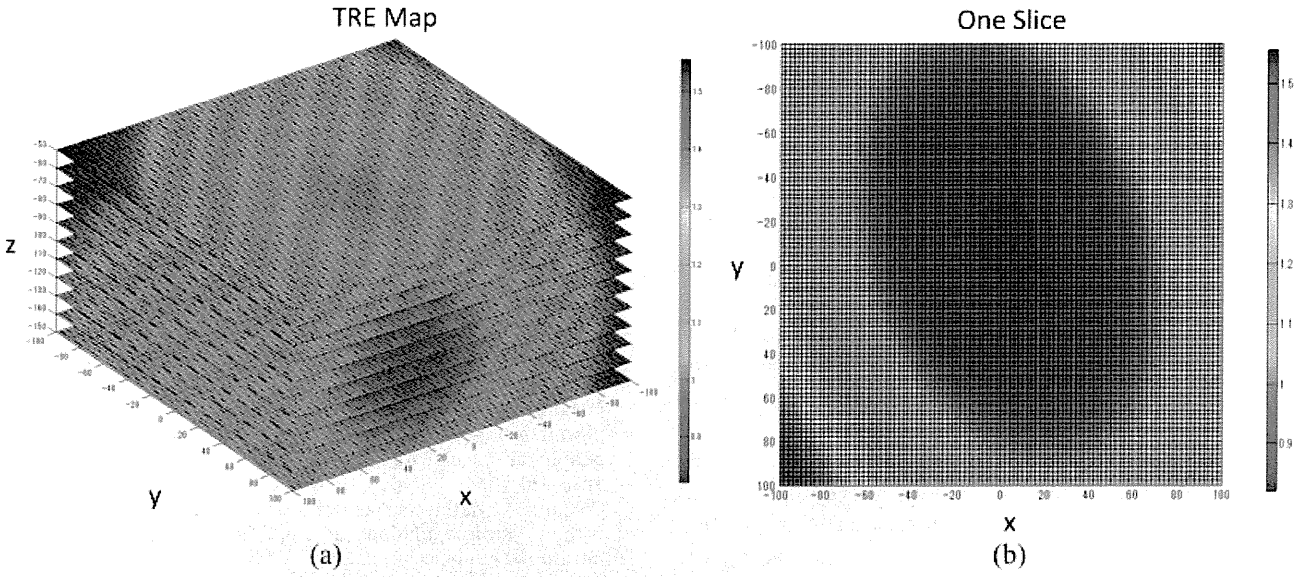

Figure 7. TRE map. The TRE map shows the RMS error of a target point when mapped through the estimated transformation matrix from the EM tracker frame to the CT image space. (a) Slices of the TRE map along the z-direction of the EM tracker frame. (b) One slice of the TRE map. The RMS error is demonstrated by the color from blue (0.8 mm) to red (1.6 mm). The configuration of the skin markers was designed so that the surgical site was located in the blue area

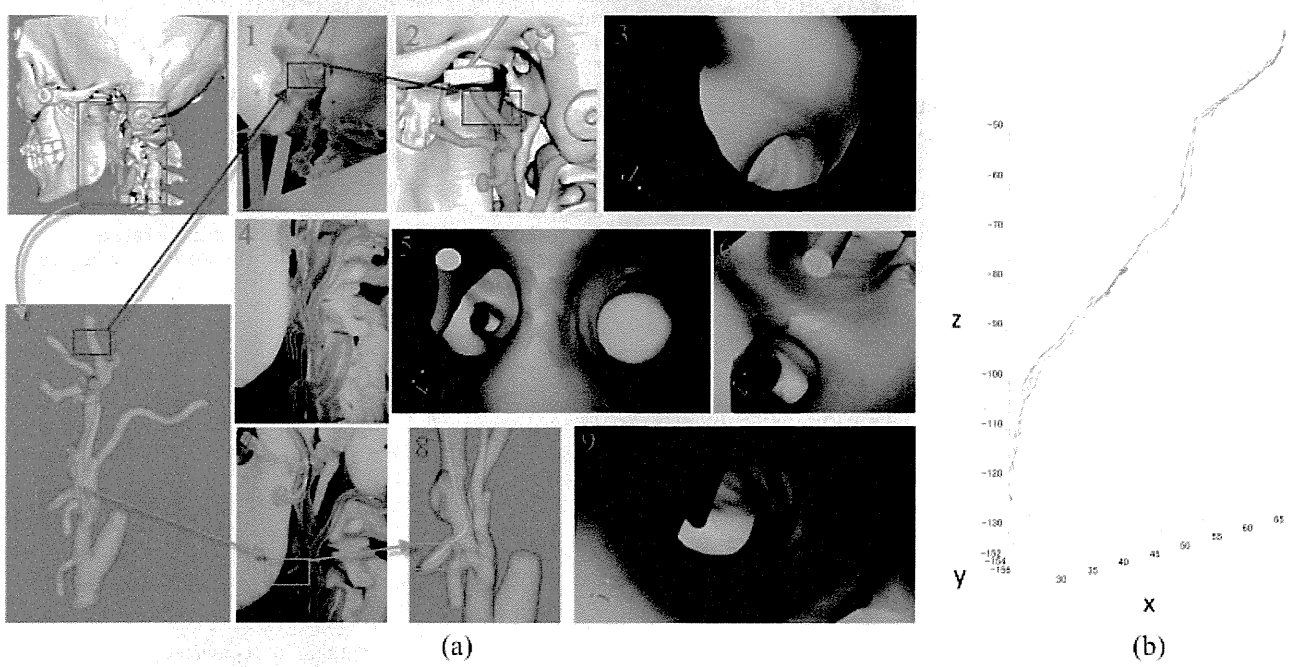

Figure 8. (a) Catheter navigation procedure and results. Picture 1: catheter with guide wire inserted into the vessel (real scene). Picture 2: the surface rendering model of the catheter indicates the current pose of the real catheter, which corresponds with Picture 1 (virtual scene). Picture 3: virtual intravascular image taken by C_B in SP1. Picture 4: the catheter being pulled out along the superficial temporal artery in SP2. Picture 5 and 6 show the virtual intravascular images taken by C_V. Picture 7 and Picture 8 show the catheter placed into the target vessel branch and Picture 9 is the virtual intravascular image taken by C_V along the facial artery centerline for verification. (b) Trace of the catheter tip in SP1. The red curve is the centerline of the external carotid artery; the blue vectors represent motions of the catheter tip during SP1

cancer treatment. The navigation system can visualize the catheter and guide the placement procedure in an intuitive way. As real-time visual feedback, the virtual intravascular video gives surgeons a good understanding of catheter manipulation; the navigational information tree organizes all navigational information well and helps surgeons operate properly; the TRE map predicts the possible error in the current position of the catheter tip. Preliminary experiments were performed to evaluate the new method and experimental results showed the effectiveness and accuracy level of the system.

In the preliminary experiment a vessel phantom rather than a real vessel was used. It seems that the problem was easier in this case because real vessels are soft and

may suffer from deformation. However, as agreed by the clinicians, in a real intervention only a small part of the vessel near to the incision on the face suffers from deformation whereas in the area of the target branch, the deformation is minimal and can be ignored. So we still believe that the method is helpful and significant. Another possible problem is skin shift, which may result in a poor registration result. Although during the intervention the patient's head is fixed, skin shift may still occur. In this paper we do not discuss skin shift but we can verify whether poor registration occurs or not by monitoring the trace of the catheter tip and its distance to the centerline during SP1. Moreover, we have noticed that the motions of the catheter are constrained within the vessel. So it is possible to reduce the navigation error by limiting the motions of the catheter model along the centerline. This can be done by shifting the tracked catheter position towards the centerline. Thus only the error along the tangent of the centerline contributes to the system error, which means an improvement in system accuracy. The result given by any navigation system should be verified by real-time imaging modalities (e.g. c-arm) if applied clinically. Whether the catheter has been positioned in the right place or not can be verified by taking a DSA image. The fact that a c-arm negatively affects the performance of an EM tracking system if it is too close to the field generator is not a problem because this step is taken only at the end of navigation. In addition, it may be very interesting to combine the proposed method with the interventional rotational C-arm 3D reconstruction. One of the most important merits of the latter is that it can produce intraoperative 3D images. If the intraoperative 3D image can be used as the anatomical atlas and an effective image registration method is available, vessel deformation and head/skin shift will be overcome.

Even though the proposed method has some benefits, we still face some challenges when delivering it to clinical interventions. These challenges include the vulnerability of the sensor coil, the size of the sensor-attached catheter, the configuration of the sensors, etc. At present, we combined the sensors and the catheter in a simple manner because of considerations of reuse; however, we are considering a special compact catheter that can be tracked directly by an EM tracking system. As a future plan, we will improve the catheter design and conduct *in vivo* animal experiments to evaluate the prototype system.

References

1. Tohnai I, Fuwa N, Hayashi Y, *et al.* New superselective intra-arterial infusion via superficial temporal artery for cancer of the tongue and tumor tissue platinum concentration after carboplatin (CBDCA) infusion. *Oral Oncol* 1998; **34**(5): 387–390.
2. Lee YY, Isaiah W, Dimery IW, *et al.* Superselective intra-arterial chemotherapy of advanced paranasal sinus tumors. *Arch Otolaryngol* 1989; **115**(4): 503–511.
3. Fuwa N, Kodaira T, Furutani K, *et al.* A new method of selective intra-arterial infusion therapy via the superficial temporal artery for head and neck cancer. *Oral Surg Oral Med Oral Pathol Oral Radiol Endod* 2008; **105**(6): 783–789.
4. Uehara M, Shiraishi T, Tobita T, *et al.* Antitumor effects on primary tumor and metastatic lymph nodes by superselectiveintra-arterial concurrent chemoradiotherapy for oral cancer. *Oral Surg Oral Med Oral Pathol Oral Radiol Endod* 2010; **110**(2): 172–177.
5. Kishi K, Matsunaka M, Sato M, *et al.* T1 and T2 lip cancer: a superselective method of facial arterial infusion therapy – preliminary experience. *Radiology* 1999; **213**(1): 173–179.
6. Tohnai I. Chemotherapy using intra-arterial infusion for oral cancer. *Nagoya J Med Sci* 2006; **68**: 101–108.
7. Bremer C, Ntziachristos V, Weissleder R. Optical-based molecular imaging: contrast agents and potential medical applications. *Eur Radiol* 2003; **13**(2): 231–243.
8. Niederhauser J, Jaeger M, Lemor R, *et al.* Combined ultrasound and optoacoustic system for real-time high-contrast vascular imaging in vivo. *IEEE Trans Med Imaging* 2005; **24**(4): 436–440.
9. Sigel B. A brief history of doppler ultrasound in the diagnosis of peripheral vascular disease. *Ultrasound Med Biol* 1998; **24**(2): 169–176.
10. Colombo A, Hall P, Nakamura S, *et al.* Intracoronary stenting without anticoagulation accomplished with intravascular ultrasound guidance. *Circulation* 1995; **91**(6): 1676–1688.
11. Chilcote WA, Modic MT, Pavlicek WA, *et al.* Digital subtraction angiography of the carotid arteries: a comparative study in 100 patients. *Radiology* 1981; **139**(2): 287–295.
12. Rubin GD, Dake MD, Napel SA, *et al.* Three-dimensional spiral CT angiography of the abdomen: initial clinical experience. *Radiology* 1993; **186**(1): 147–152.
13. Hautmann H, Schneider A, Pinkau T, *et al.* Electromagnetic catheter navigation during bronchoscopy: validation of a novel method by conventional fluoroscopy. *Chest* 2005; **128**: 382–387.
14. Tanase D, Goosen GFL, Trimp PJ, French PJ. Multi-parameter sensor system with intravascular navigation for catheter/guide wire application. *Sensor Actuat A – Phys* 2002; **97–98**: 116–124.
15. Solonmon SB, Dickfeld T, Calkins H. Real-time cardiac catheter navigation on three-dimensional CT images. *J Interv Card Electr* 2003; **8**: 27–36.
16. Schneider MAE, Ndrepepa G, Dobran I, *et al.* LocaLisa catheter navigation reduces fluoroscopy time and dosage in ablation of atrial flutter: a prospective randomized study. *J Cardiovasc Electr* 2003; **14**(6): 587–590.
17. Ramcharitar S, Pugliese F, Schultz C, *et al.* Integration of multi-slice computed tomography with magnetic navigation facilitates percutaneous coronary interventions without additional contrast agents. *J Am Coll Cardiol* 2009; **53**(9): 741–746.
18. Doris HU, Richar HB. Interpolating splines with local tension, continuity, and bias control. *Comput Graphics* 1984; **18**(3): 33–41.
19. Saito T, Toriwaki J. New algorithm for euclidean distance transformation of an N-dimensional digitized picture with applications. *Pattern Recogn* 1994; **27**(11): 1551–1565.
20. Wan M, Liang ZR, Ke Q, *et al.* Automatic centerline extraction for virtual colonoscopy. *IEEE Trans Med Imaging* 2002; **21**(12): 1450–1460.
21. Silverman BW. Spline smoothing: the equivalent variable kernel method. *Ann Stat* 1984; **12**: 898–916.
22. Robb RA. Virtual endoscopy: development and evaluation using the visible human datasets. *Comput Med Imag Graph* 2000; **24**(3): 133–151.
23. Schonemann PH. A generalized solution of the orthogonal procrustes problem. *Psychometrika* 1966; **31**(1): 1–10.
24. Arun KS, Huang TS, Blostein SD. Least squares fitting of two 3-D point sets. *IEEE Trans Pattern Anal* 1987; **9**: 698–700.
25. Horn BKP. Closed-form solution of absolute orientation using unit quaternions. *J Opt Soc Am* 1987; **5**(7): 1127–1135.
26. Horn BKP, Hilden HM, Negahdaripour S. Closed-form solution of absolute orientation using orthonormal matrices. *J Opt Soc Am* 1988; **4**(7): 629–642.
27. Frantz DD, Wiles AD, Leis SE, Kirsch SR. Accuracy assessment protocols for electromagnetic tracking systems. *Phys Med Biol* 2003; **48**: 2241–2251.
28. Moghari MH, Abolmaesumi P. Point-based rigid-body registration using an unscented Kalman filter. *IEEE Trans Med Imaging* 2007; **26**(12): 1708–1728.

29. Fitzpatrick JM, West JB, Maurer CR. Predicting error in rigid-body point-based registration. *IEEE Trans Med Imaging* 1998; **17**(5): 694–702.
30. Moghari MH, Abolmaesumi P. A high-order solution for the distribution of target registration error in rigid-body point-based registration. In *Lecture Notes Computer Science, MICCAI 2006*. Berlin: Springer-Verlag; 603–611.
31. Ma B, Moghari MH, Ellis RE, Abolmaesumi P. On fiducial target registration error in the presence of anisotropic noise. In *Lecture Notes Computer Science, MICCAI 2007*. Berlin: Springer-Verlag; 628–635.

Cardiovasc Intervent Radiol (2011) 34:S321–S323
DOI 10.1007/s00270-010-0053-2

LETTER TO THE EDITOR

Endovascular Repair of a Perforation of the Vena Caval Wall Caused by the Retrieval of a Gunther Tulip Filter After Long-Term Implantation

Hiroyuki Morishita · Takuji Yamagami · Tomohiro Matsumoto · Yoshito Takeuchi · Osamu Sato · Tsunehiko Nishimura

Received: 7 August 2010 / Accepted: 24 October 2010 / Published online: 8 December 2010

Abstract Symptomatic penetration of the inferior vena cava (IVC) wall reportedly occurs in 0.3% of patients in whom a filter has been implanted, and it causes injury to the adjacent structures (Bogue et al. in Pediatr Radiol 39(10): 1110–1113, 1; Brzezinski et al. in Burns 32(5):640–643, 2). We succeeded in the endovascular repair of perforation of the IVC wall occurring during the retrieval of a penetrated Gunther tulip vena cava filter (Cook, Bjaeverskov, Denmark) after long-term implantation.

Case Report

A 67-year-old woman with acute right-sided back pain was admitted to our hospital. She had a medical history of surgery for ovarian cancer and uterine endometrial cancer. After the operation, pulmonary embolism (PE) and deep venous thrombus (DVT), distributed from the left popliteal vein to the left external iliac vein, developed. Her left leg was swollen due to DVT. To avoid worsening of the PE, a Gunther tulip vena cava filter (GTF; Cook, Bjaeverskov, Denmark) was inserted. At that time, it was planned to be used as a permanent filter. Since then she had been administered warfarin. The international normalized ratio (INR) was maintained between 2.0 and 2.5.

Two hundred ninety-eight days after implantation of the filter, contrast-enhanced computed tomography (CT) demonstrated massive fluid accumulation in the right perirenal space, resulting from perforation of the IVC wall and right renal pelvis due to penetration of the GTF. It was also shown that the hook of the penetrating GTF contacted the wall of the aorta. There was no hemorrhage around the IVC. We considered that the GTF should be retrieved because the perforation was symptomatic, and there was a risk that the penetrating hook would cause a fatal aortic injury. It was considered difficult to retrieve the GTF with an endovascular procedure because the hook was embedded in the wall of the IVC, and there was a marked possibility of perforating the IVC wall. Thus, it was decided to refer the patient for open surgery. However, she did not agree to the surgical treatment plan and selected endovascular therapy.

Endovascular retrieval was performed as follows. The day before the procedure, the administration of warfarin was stopped, and vitamin K was administered to decrease the effect of the warfarin. As a result, her INR was normalized to 1.0. GTF retrieval was undertaken by way of the right internal jugular vein. A vena cavogram showed that the filter had tilted to the left wall and that the hook and right strut had penetrated the IVC wall (Fig. 1). First, we attempted retrieval with the standard Gunther Tulip Vena Cava Filter Retrieval Set (Cook). However, we failed to snare the hook of the GTF, which was embedded in the IVC wall. Subsequently, we tried to pull back the penetrated hook into the inner lumen by tangling the GTF strut with the 6F hook-shaped guiding catheter (Medikit, Tokyo,

H. Morishita (✉) · T. Matsumoto · O. Sato
Department of Diagnostic Radiology, Japanese Red Cross Kyoto Daiichi Hospital, 15-749 Honmachi, Higashiyama, Kyoto 605-0981, Japan
e-mail: hmorif@koto.kpu-m.ac.jp; mori_h33@xa2.so-net.ne.jp

T. Yamagami · T. Nishimura
Department of Radiology, Graduate School of Medical Science, Kyoto Prefectural University of Medicine, 465 Kajii-cho, Kamigyou, Kyoto 602-8566, Japan

Y. Takeuchi
Division of Diagnostic Radiology, National Cancer Center: Tsukiji Campus Hospital, 15-749 Honmachi, Higashiyama, Tokyo 104-0045, Japan

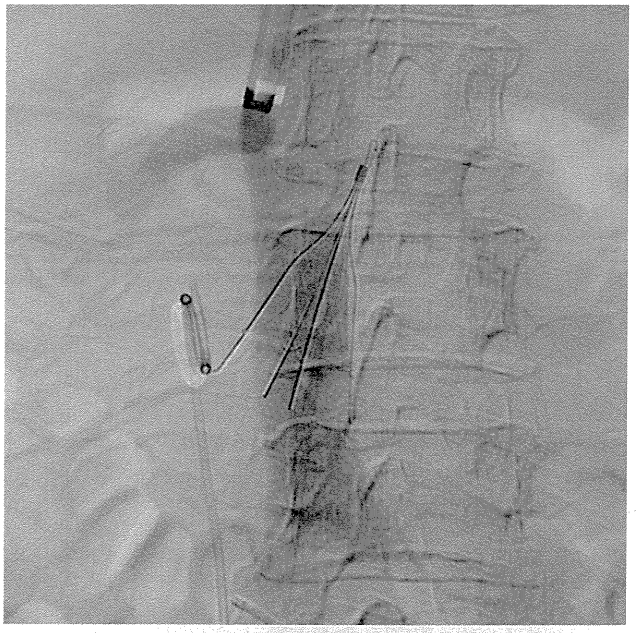

Fig. 1 A vena cavogram shows the filter tilted toward the left wall. The hook and right strut penetrate the wall of the IVC. The right strut is in contact with the double-J ureteral stent inserted in the right renal pelvis

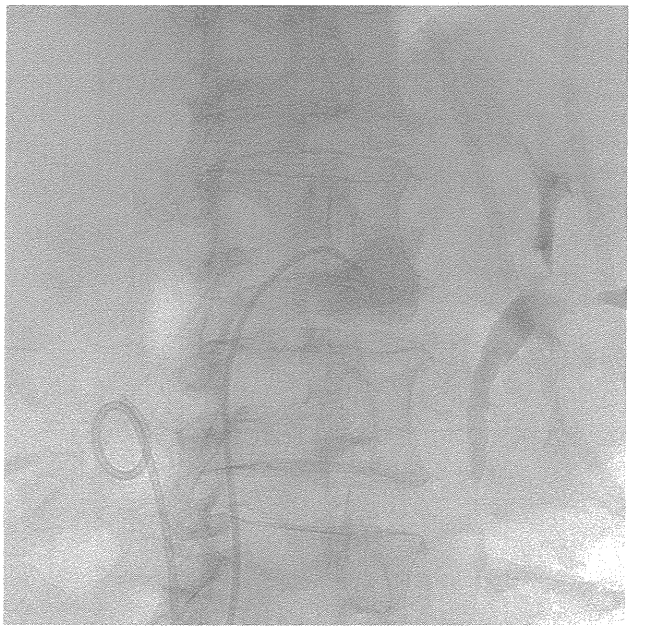

Fig. 2 A 5F cobra-shaped catheter is catheterized into the perforated hole of the IVC wall. Injected contrast medium has spread outside the IVC wall

Japan), but we again failed. Finally, we succeeded in retrieving the GTF by employing the snared-loop technique [1]. After retrieval, a vena cavogram showed extravasation from the IVC wall where the hook had penetrated. A 5F cobra-shaped catheter (Terumo, Tokyo, Japan), inserted by way of the right femoral artery, was catheterized into the perforated hole. A small amount of contrast medium was injected, which spread outside of the IVC (Fig. 2). The injured region was close to the point where the left renal vein entered. Twenty minutes after retrieval, she was stable and her vital signs were normal. We considered that open surgery was not necessary but that some kind of endovascular repair should be performed because subsequent anticoagulation was needed for her residual DVT and hypercoagulable state, which can enhance the risk of bleeding complications. To embolize the hole, we injected 1.0 ml of a mixture of N-butyl-2-cyanoacrylate (NBCA) (Histoacryl; B. Braun, Melsungen, Germany) and iodized oil (Lipiodol; Guerbet, Aulnay-sous-Bois, France) (the ratio of NBCA to Lipiodol was 1:1.5) rapidly through the 5F catheter (Fig. 3). After embolization, extravasations disappeared on vena cavogram. Immediately after the procedure, abdominal CT scan was performed, which revealed that the mixture had spread and coated the surface of the IVC wall and that there were no hemorrhage (Fig. 4). On the next day and 17 days after the procedure, abdominal CT showed that the NBCA–Lipiodol mixture around the IVC wall was stable and that there were no hemorrhage.

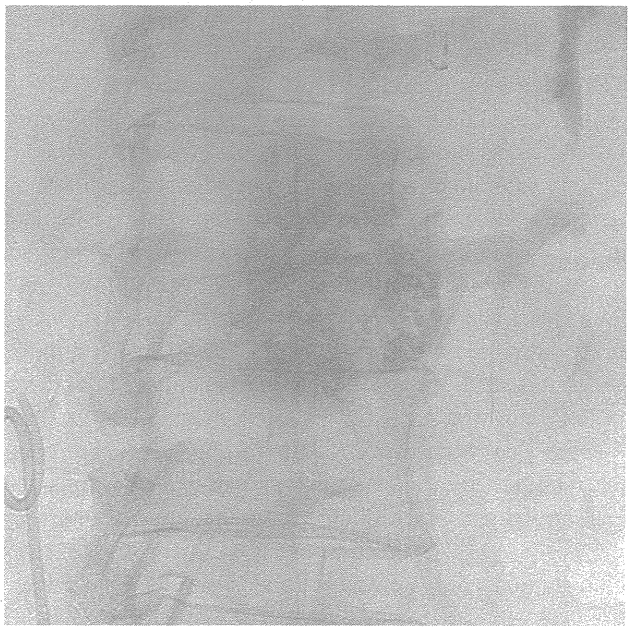

Fig. 3 The NBCA–Lipiodol mixture shows accumulation around the IVC

Discussion

Cook, the manufacturer of the GTF, initially recommended a retrieval interval of no more than 10 days. In some previous reports, the maximal recommended retrieval

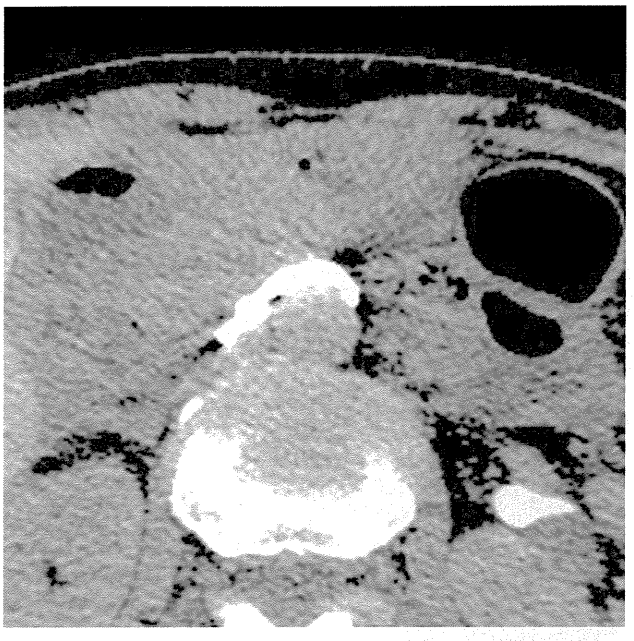

Fig. 4 On the CT scan performed after the procedure, the NBCA–Lipiodol mixture coats the surface of the IVC wall from the anterior to the left lateral side, and no hemorrhage is seen

interval was 10 to 14 days [2–4]. Millward et al. [5] noted that the maximal dwell time before successful retrieval was 25 days, and recently, Binkert et al. [6] reported a dwell time of 317 days. In our case, the retrieval interval was 298 days, which is usually too long. However, we had to perform the endovascular retrieval because of the symptom, the risks, and the patient's request.

Many techniques have been reported in cases in which filter retrieval employing the standard methods failed. In our case, we failed to retrieve it using a standard technique, but we succeeded in retrieval using the snared-loop technique [1], which is an effective and less-aggressive retrieval option and is robust enough to withstand the force needed to detach the embedded and penetrated hook from the IVC wall.

There have been many reports of clinically asymptomatic retroperitoneal hematoma caused by an implanted vena cava filter, which does not require surgical intervention [7, 8]. However, in our case, extravasation was demonstrated, and the patient had a risk of hemorrhage due to subsequent anticoagulation; thus, we attempted embolization.

We chose NBCA as an embolic agent because it is a permanent embolic material, and its adhesion time can be regulated flexibly according to the ratio of NBCA to Lipiodol [9]. We decided on the ratio of NBCA to Lipiodol of 1: 1.5 to embolize the perforation rapidly.

The present case showed that embolization is acceptable for repairing a perforation after the endovascular retrieval of a penetrating GTF.

Conflict of interest None

References

1. Doody O, Noë G, Given MF et al (2009) Assessment of snared-loop technique when standard retrieval of inferior vena cava filters fails. Cardiovasc Intervent Radiol 32(1):145–149
2. Looby S, Given MF, Geoghegan T et al (2007) Gunther Tulip retrievable inferior vena caval filters: indications, efficacy, retrieval, and complications. Cardiovasc Intervent Radiol 30(1): 59–65
3. Neuerburg JM, Gunther RW, Vorwerk D et al (1997) Results of a multicenter study of the retrievable tulip vena cava filter: early clinical experience. Cardiovasc Intervent Radiol 20:10–16
4. Yamagami T, Kato T, Hirota T et al (2007) Evaluation of retrievability of the Gunther tulip vena cava filter. Cardiovasc Intervent Radiol 30(2):226–231
5. Millward SF, Oliva VL, Bell SD et al (2001) Gunther tulip retrievable vena cava filter: results from the registry of the Canadian Interventional Radiology Association. J Vasc Interv Radiol 12:1053–1058
6. Binkert CA, Bansal A, Gates JD (2005) Inferior vena cava filter removal after 317-day implantation. J Vasc Interv Radiol 16(3): 395–398
7. Bogue CO, John PR, Connolly BL et al (2009) Symptomatic caval penetration by a Celect inferior vena cava filter. Pediatr Radiol 39(10):1110–1113
8. Brzezinski M, Schmidt U, Fitzsimons MG (2006) Acute and massive hemorrhage due to caval perforation by an inferior vena cava filter—absolute indication for surgery? Case report and review of literature. Burns 32(5):640–643
9. Yamagami T, Kato T, Iida S et al (2004) Value of transcatheter arterial embolization with coils and n-butyl cyanoacrylate for long-term hepatic arterial infusion chemotherapy. Radiology 230: 792–802

Cardiovasc Intervent Radiol
DOI 10.1007/s00270-011-0294-8

TECHNICAL NOTE

A New Flow Control Technique Using Diluted Epinephrine in the *N*-butyl-2-cyanoacrylate Embolization of Visceral Artery Pseudoaneurysms Secondary to Chronic Pancreatitis

Hiroyuki Morishita · Takuji Yamagami · Yoshito Takeuchi · Tomohiro Matsumoto · Shunsuke Asai · Koji Masui · Hideki Sato · Fumihiro Taniguchi · Osamu Sato · Tsunehiko Nishimura

Received: 19 July 2011 / Accepted: 5 October 2011

Abstract Although *n*-butyl-2-cyanoacrylate (NBCA) has been used as an effective liquid embolization material, its indication for pseudoaneurysms has seemingly been limited because of the technical difficulties of using NBCA, such as reflux to the parent artery and causing significant infarction. Thus, considerable skill in using NBCA or a device to control blood flow during its polymerization is required to achieve embolization without severe complications. We report our new technique for controlling blood flow using diluted epinephrine in transcatheter arterial NBCA embolization of five pseudoaneurysms in four cases secondary to hemosuccus pancreaticus.

H. Morishita (✉) · T. Matsumoto · S. Asai · K. Masui · O. Sato
Department of Diagnostic Radiology, Japan Red Cross Kyoto Daiichi Hospital, 15-749 Honmachi, Higashiyama, Kyoto 605-0981, Japan
e-mail: hmorif@koto.kpu-m.ac.jp; mori_h33@xa2.so-net.ne.jp

T. Yamagami · T. Nishimura
Department of Radiology, Graduate School of Medical Science, Kyoto Prefectural University of Medicine, 465 Kajii-cho, Kamigyou, Kyoto 602-8566, Japan

Y. Takeuchi
Division of Diagnostic Radiology, National Cancer Center, Tsukiji Campus Hospital, 5-1-1 Tsukiji, Chuo, Tokyo 104-0045, Japan

H. Sato
Department of Gastroenterology, Japan Red Cross Kyoto Daiichi Hospital, 15-749 Honmachi, Higashiyama, Kyoto 605-0981, Japan

F. Taniguchi
Department of Surgery, Japan Red Cross Kyoto Daiichi Hospital, 15-749 Honmachi, Higashiyama, Kyoto 605-0981, Japan

Keywords Chronic pancreatitis · Pseudoaneurysm · Transcatheter arterial embolization · Epinephrine · *n*-butyl-2-cyanoacrylate · Flow control

Introduction

Hemosuccus pancreaticus, which is defined as gastrointestinal bleeding via the pancreatic duct and duodenal papilla, is a rare cause of gastrointestinal bleeding with diagnostic difficulties, and is sometimes life-threatening [1]. The bleeding is caused by the rupture of a pseudoaneurysm, which results from weakening of the arterial wall caused by partial enzymatic digestion and pressure necrosis due to the pancreatic pseudocyst [2]. Most cases are diagnosed by contrast-enhanced computed tomography (CT) or angiography [1–3]. As a therapeutic method for a bleeding pseudoaneurysm secondary to chronic pancreatitis, Kirby et al. [4] concluded that prompt angiography and endovascular embolization should be selected, Udd et al. [5] concluded that all hemodynamically stable patients should undergo prompt initial angiographic evaluation and embolization if possible, and Bergert et al. [6] concluded that embolization remains the definitive treatment if there are no other pancreas-related indications for surgery. So, when a patient is hemodynamically stable or there are no indications for surgery, prompt endovascular therapy should be selected. Several techniques of endovascular treatment for pseudoaneurysms have been reported in the literature: (1) embolization proximal to the pseudoaneurysm; (2) embolization of the aneurysm neck; (3) intra-aneurysmal glue embolization; (4) embolization of vessels both distal and proximal to the pseudoaneurysm; and (5) sac packing with detachable coils [1–9].

In this technical report, we describe our initial experience of flow control using diluted epinephrine in *n*-butyl-2-

Published online: 25 October 2011

cyanoacrylate (NBCA; Histoacryl, B. Braun, Tuttlingen, Germany) embolization of five pseudoaneurysms in four patients with hemosuccus pancreaticus. We have retrospectively reviewed these cases to evaluate the feasibility and usefulness of this new flow control technique developed by us.

Materials and Methods

Between January 2008 and March 2011, four male patients, aged 46–60 (mean, 53) years, were admitted to our hospital with upper abdominal pain and repeated black-colored stools. They all had a history of alcoholic chronic pancreatitis. One had a history of colon cancer and had been under treatment for multiple liver metastases. On admission, their complete blood counts showed anemia. In all patients, upper gastrointestinal endoscopy and colonoscopy failed to identify the site of hemorrhage, and abdominal noncontrast and contrast-enhanced CT revealed worsening of the chronic pancreatitis with a pseudoaneurysm. The origin of the hemorrhage was considered to be rupture of the pseudoaneurysm. A total of five pseudoaneurysms showed in four cases: two at the splenic artery; one at the posterior pancreaticoduodenal artery; and one at the splenic and the anterior pancreaticoduodenal artery. The characteristics of the patients are shown in Table 1. In three cases, the pseudoaneurysm had ruptured into the pseudocyst. Two patients were in a state of hemorrhagic shock, and, furthermore, one of the two others showed disseminated intravascular coagulation.

For these four patients, we performed emergent transcatheter arterial embolization (TAE) of the pseudoaneurysm. After being informed about the procedure, risk, and complications, written informed consent was obtained from the patients.

Procedure

The procedure was performed under local anesthesia via a right femoral approach. The pseudoaneurysm was catheterized selectively using a 2.2-F microcatheter (Progreat, Terumo, Tokyo, Japan) introduced coaxially through a 5-F shepherd-hook or cobra-2 shaped catheter (Terumo, Tokyo, Japan). Angiography revealed a pseudoaneurysm. As a therapeutic method, we selected packing of the pseudoaneurysm and complete isolation from the parent circulation. We chose NBCA as an embolic agent, because we are accustomed to using NBCA in embolization for arterial bleeding. Reflux or an overflow of NBCA might cause significant complications, such as splenic infarction, pancreatic infarction, and mesenteric ischemia, if blood flow is not controlled. However, we were afraid that

Table 1 Characteristics of patients with hemosuccus pancreaticus and results of embolization

Patient (gender/age/yr)	Hb (g/dl)/Hct (%)	HR (pulese/min)/BP (mmHg)	Location of PS	Volume of PS on CT (ml)	Volume of diluted epinephrin e (ml)	Injected NBCA-Lp (ml)	Technical success	Significant complications	Total follow-up length by CT	Recurrence
1/m/46	6.0/20.1	88/ 122–74	Splenic A.	1.87 (18 × 11 × 18 mm)	5	1	Yes	None	N/A[a]	-
2/m/57	7.7/24	160 106–56	Splenic A.	5.8 (22 × 22 × 23 mm)	10	2.5	Yes	None	30 mo	None
3/m/50	11.5 /36	77/114–80	Pancreaticoduodenal A.	1.31 (16 × 12 × 13 mm)	5	1	Yes	None	25 mo	None
4/m/60	8.4/25	114/102–60	Splenic A.	1.06 (15 × 9 × 15 mm)	5	0.6	Yes	None	N/A[b]	
			Pancreaticoduodenal A.	0.28 (12 × 6 × 7.5 mm)	2.5	0.2	Yes	None		

Hb hemoglobin; *Hct* hematocrit; *HR* heart rate; *BP* blood pressure; *A* artery; *NBCA* n-butyl-2-cyanoacrylate; *LP* lipiodol; *PS* pseudoaneurysm

PS sizes are calculated using the formula for an ellipsoid: a × b × c × $\pi/6$, where a is the maximum length of PS. and b and c are the maximum widths in the two transverse dimensions

[a] Due to moving to a distant place

[b] Death by cerebral hemorrhage

CT was performed every 6 months

inflation of the balloon might rupture the vascular wall, which was damaged by the pancreatitis. Therefore, to control blood flow, we selected the injection of diluted epinephrine, which strongly constricts the distal and proximal side vessels of the parent artery and makes it possible both to avoid the excessive overflow of NBCA and to embolize the distal and proximal sides of the parent artery without significant complications.

The procedure was performed as follows (Fig. 1):

(1) To assess the volume of the pseudoaneurysm, we injected the contrast material until it overflowed to the parent artery, through the microcatheter, which was catheterized within the pseudoaneurysm.
(2) We diluted 0.01 mg of epinephrine (Bosmin, 1 mg/ml, Daiichi-Sankyo, Tokyo, Japan) with heparinized saline (1,000 IU of heparin was diluted with 500 ml of saline), the volume of which was sufficient to overflow from the pseudoaneurysm. Then, we injected it through the microcatheter. Immediately after overflow of the diluted epinephrine from the pseudoaneurysm, it flowed to the distal side of the parent artery, which was constricted and narrowed. Then, the diluted epinephrine was refluxed to the proximal side. As a result, both the proximal and distal sides of the parent artery were constricted, and the pseudoaneurysm was isolated from the blood flow.
(3) We injected the contrast medium to confirm that there was no overflow to the parent artery. If considerable overflow is detected, the additional diluted epinephrine should be injected. However, this was not required in any of the cases presented; therefore, 0.01 mg of epinephrine in total was injected in all cases.
(4) After confirmation, we flushed the microcatheter with 5 ml of 5% glucose solution to prevent premature polymerization of the tissue adhesive.
(5) Under fluoroscopy, we injected a 33% mixture of NBCA and lipiodol (Guerbet, Aulnay-sous-Bois, France) to fill the pseudoaneurysm and intentionally overflowed a small amount of the mixture to the parent artery that was enough to embolize both proximal and distal sides.
(6) The microcatheter was pulled back immediately following the injection of NBCA to avoid inadvertent adherence to the vascular wall. Steps 4 and 5 were performed within 45–80 s, which is the reported

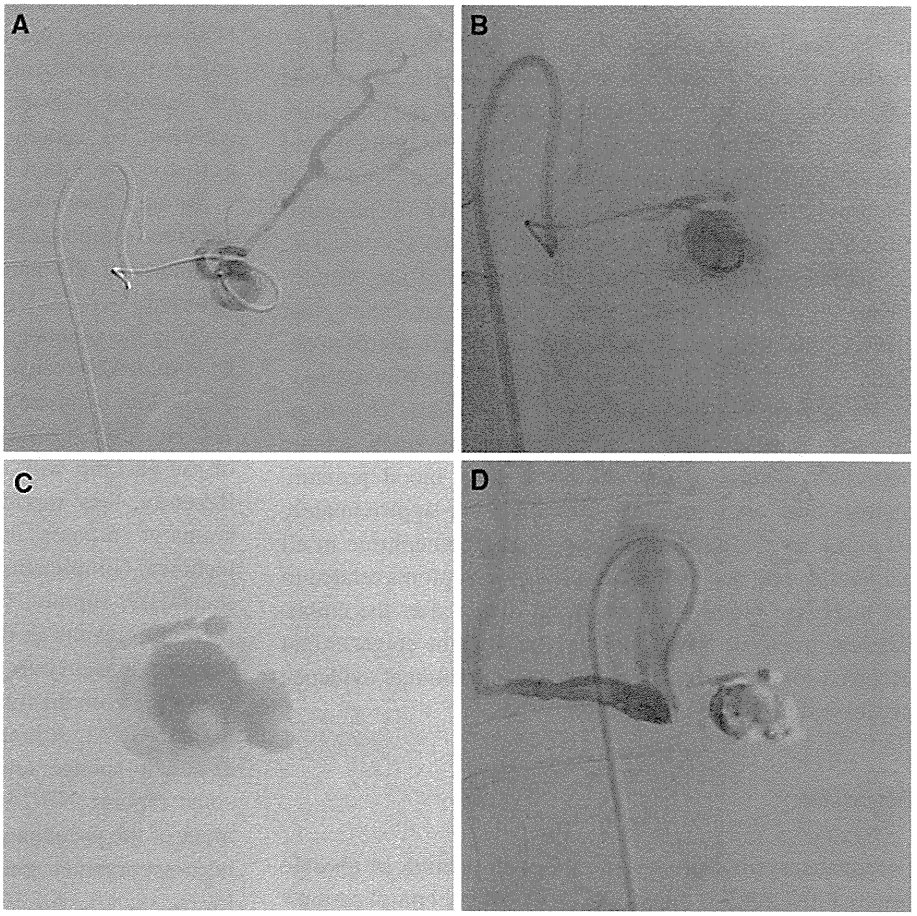

Fig. 1 A 60-year-old male with hemosuccus pancreaticus. **A** Angiography shows a pseudoaneurysm of the splenic artery catheterized with microcatheter. Note the tip of the microcatheter within the pseudoaneurysm. **B** After the injection of diluted epinephrine, the injected contrast medium is accumulating in the pseudoaneurysm, and the overflowed contrast medium is stagnant in the parent artery. **C** After the embolization, NBCA and lipiodol mixture is accumulating in the pseudoaneurysm, and the proximal and distal sides of the parent artery to the pseudoaneurysm. **D** In celiac axis arteriogram after embolization, the splenic artery is not visualized